Accepted Manuscript in Solar Energy 169, 34-39

Gabriel López, Christian A. Gueymard, Juan Luis Bosch, Igor Rapp-Arrarás, Joaquín Alonso-Montesinos, Inmaculada Pulido-Calvo, Jesús Ballestrín, Jesús Polo, Javier Barbero. 2018. Modeling water vapor impacts on the solar irradiance reaching the receiver of a solar tower plant by means of artificial neural networks. Solar Energy 169, 34-39. DOI: 10.1016/j.solener.2018.04.023

Link to published version:
https://www.sciencedirect.com/science/article/abs/pii/S0038092X18303682?via%3Dihub

Modeling water vapor impacts on the solar irradiance reaching the receiver of a solar tower plant by means of Artificial Neural Networks

Gabriel López[1], Christian A. Gueymard[2], Juan Luis Bosch[1], Igor Rapp-Arrarás[3], Joaquín Alonso-Montesinos[4], Inmaculada Pulido-Calvo[3], Jesús Ballestrín[5], Jesús Polo[6] and Javier Barbero[4]

[1] Dpto. Ingeniería Eléctrica y Térmica, de Diseño y Proyectos, Universidad de Huelva, Huelva (Spain)

[2] Solar Consulting Services, P.O. Box 392, Colebrook, NH 03576 (USA)

[3] Dpto. Ciencias Agroforestales, Universidad de Huelva, Huelva (Spain)

[4] Dpto. Química y Física, University of Almería, Almería (Spain)

[5] Concentrating Solar System Unit (Plataforma Solar de Almería, CIEMAT), Almería (Spain)

[6] Photovoltaic Solar Energy Unit (Renewable Energy Division, CIEMAT), Madrid (Spain)

Abstract

This work analyses the influence of water vapor on the atmospheric transmission loss of solar radiation between heliostats and the receiver of solar power tower plants. To this purpose, an atmospheric transmission code (MODTRAN) is used to generate values of direct normal irradiance (DNI) reaching the mirror and the receiver under different geometries (including sun position, tower height, and mirror-to-receiver slant range) and atmospheric conditions related to water vapor and aerosols. These variables are then used as inputs to an artificial neural network (ANN), which is trained to calculate the corresponding DNI attenuation. Two different aerosol scenarios are simulated: an ideal aerosol-free atmosphere, and a widely different one corresponding to semi-hazy conditions. The developed ANN model is then able to provide the DNI attenuation over a wide range of the input variables considered here, with root mean square differences of only 0.8%. The transmission loss due to water vapor is found to decrease with sun elevation. This is explained by the saturation effect in the incident irradiance at the mirror. The simplicity and accuracy of the algorithm are its great strengths, allowing its anticipated inclusion into the actual energy simulation codes currently used for solar tower plant design.

Keywords: *solar power towers, transmission losses, water vapor, artificial neural networks*

1. Introduction

Estimation of direct normal irradiance (DNI) is a research topic of increasing interest in solar energy, particularly for concentrating solar power (CSP) production. Power generation from Solar Power Towers (SPT), for which DNI is a critical input, is experiencing a rapid growth worldwide, linked to a rapid increase in the generated power and quasi-baseload opportunities offered by high-temperature heat storage. It is anticipated that the SPT technology will be one of the main contributors to the future mix of renewable energies. The greater challenges posed by these large solar installations is their complexity and cost.

Economies of scale are possible, but require large installations, where the outer heliostats can be a few kilometers away from the receiver. To guarantee a good design and estimate of the electricity production under any circumstances, it is crucial to have an accurate evaluation of the DNI received by the receiver from each heliostat at any instant, since this ultimately affects the operation and revenue, as well as the energy price market.

Under cloudless conditions, aerosols and water vapor have relatively high concentrations near the ground and thus are the main variable atmospheric constituents attenuating the DNI after reflection by heliostats. As a matter of fact, experience has shown that the heliostat-to-tower attenuation can reach substantial levels in cases of high turbidity and/or humidity content near ground level. For instance, Saharan dust outbreaks in southern Spain are not rare, and produce significant attenuation levels. Figure 1 clearly illustrates the optical effect of such an event, which occurred in February 2016 at the Plataforma Solar de Almería (PSA) research center (Spain). That specific event and ensuing DNI attenuation are further analyzed by Alonso-Montesinos et al. (2017).

Fig. 1: Low visibility and substantial light scattered by large particles in the atmosphere at PSA on 2016-02-22 at 14:30 local time. Solar radiation reflected by the heliostats is visibly attenuated by scattering.

The above-mentioned dust outbreaks occur several times a year, affecting the production of all solar tower plants installed in Andalusia, in particular. Such episodes are even more frequent in northern Africa, the Middle East, or Asia, where a rapid growth in the number of installed SPT plants is expected. Consequently, the specialized computer codes commonly used by engineers for plant sizing or energy simulation of SPT systems should include the effects of these extreme atmospheric conditions, while being also flexible and general in order to be used under a variety of climates, etc. Unfortunately, the models that can estimate such losses were typically developed several decades ago (Vittitoe and Biggs, 1978; Pitman and Vant-Hull, 1982), and are insufficient to meet the increased accuracy demanded by new SPT projects. Ballestrín and Marzo (2012) have compared the atmospheric mirror-to-receiver (MTR) attenuation results from the above-mentioned simple algorithms to detailed simulations obtained with the rigorous MODTRAN atmospheric spectral code (Berk et al., 1989) for a rural-type atmosphere. Although the Pitman and Vant-Hull model showed good results, both for turbid and clean conditions, only two different turbidity conditions were simulated, which is far from representing all possible conditions

at any one SPT site.

In perspective, it is important to estimate the direct value of better evaluating atmospheric attenuation losses. The sizing of the heliostats field using different SPT design codes such as DELSOL or MIRVAL can present deviations up to 4% when considering variable conditions of aerosols and water vapor, leading to significant economic repercussions (Cardemil et al., 2014). Polo et al. (2017) have found differences of up to 20% in the energy output production of large SPT plants depending on the time-scale input information (e.g. daily, monthly or yearly values) used to model the atmospheric extinction. These findings support the need of analyzing and modeling the effects of different atmospheric components, such as aerosols or water vapor, on the MTR attenuation at fine temporal resolution. Theoretical simulations conducted by means of spectral radiative codes, such as MODTRAN, show that reductions up to 30% in solar irradiance incident on distant heliostats can occur under moderately turbid conditions (López et al., 2017).

In recent years, methods for the direct or indirect experimental determination of the horizontal extinction coefficient or of the energy attenuation have been proposed. For instance, Sengupta and Wagner (2012) proposed to derive the MTR attenuation from the measurement of DNI with two pyrheliometers, one measuring the incident DNI on the mirror (or heliostat), and the other one measuring the DNI incident on the receiver. The authors noted the great difficulties inherent to this methodology (depending on the reflectance of mirrors, their cleanliness variations in local conditions, etc.), and the crucial importance of measurement errors. Tahboub et al. (2014) used measurements from four pyrheliometers installed on the side of a mountain and staggered at various elevations (from 340 to 1035 m) to study the correlation between the DNI measurements thus obtained at different heights. More generally, a thorough review of experimental methods and atmospheric attenuation models can be found in the recent literature (Hanrieder et al., 2017). Even though the current knowledge points at aerosols as the main source of slant MTR attenuation, there is no exhaustive study analyzing the relative importance of other atmospheric variables, such as water vapor, and their effects on energy losses.

In this work, the radiation losses specifically caused by air molecules and water vapor are analyzed, and a preliminary soft-computing algorithm is proposed to evaluate them with sufficient accuracy. To that end, the spectral propagation of DNI from the top of the atmosphere to the receiver is simulated with MODTRAN for several air masses, also taking the atmospheric composition into account. The dependence of the attenuated DNI on solar zenith angle, amount of water vapor, MTR distance, and others factors, is analyzed toward the development of a general prediction model.

Using conventional methods, the complex non-linear relationships between the various atmospheric or geometric inputs and transmission loss lead to excessive difficulties in finding a suitable mathematical function. An artificial neural network (ANN) is thus rather developed here to obtain transmission loss estimates from the inputs considered. In addition to the multiple applications of ANN methods in pattern recognition and classification, function approximation, prediction, etc., their usage in data analysis is growing fast, offering an effective alternative to more traditional techniques in many scientific fields. Particularly, in the meteorological and solar energy resource fields, ANN-based methods have been

successfully developed to evaluate various solar radiation variables, thus improving their accuracy with respect to more conventional statistical approaches (Bosch et al., 2008; Eissa et al., 2013; López and Gueymard, 2007; Srikrishnan et al., 2015). Moreover, ANNs are starting to be used to estimate solar irradiance with a similar degree of accuracy as what can be achieved by the more conventional methods based on broadband or spectral radiative models (Takenaka et al., 2011; Taylor et al., 2016). Thus, this emerging application of ANN allows efficient (fast and accurate) calculations of the otherwise computationally expensive and complex mathematical formulations involved when using conventional spectral radiative transfer models.

2. Methodology

2.1. Generation of synthetic data

The MODTRAN model is used here to obtain hundreds of initial predictions of the incident DNI, both at the mirror M (E_M) and at the receiver on the tower T (E_T), after E_M is reflected by M (Fig. 2). These simulations pertain to a large range of solar zenith angles (Θ_z), mirror-to-receiver slant ranges (S), tower heights (H), precipitable water (w), and two widely different turbidity conditions. These initial, spectrally-based predictions are used as the foundation of the proposed ANN model.

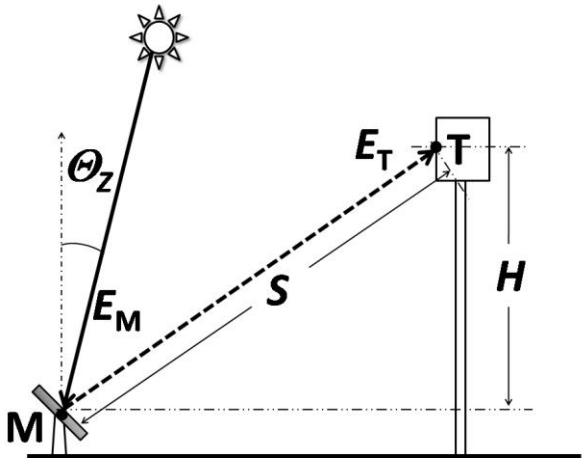

Fig. 2: Schematic description of the tower power plant and nomenclature.

As modeled in MODTRAN, the spectral transmittance between M and T is an intricate function of line-of-sight geometry, aerosol characteristics (such as type of aerosol or type of aerosol extinction), water vapor content, amounts of absorbing gases (ozone, carbon dioxide, etc.), and various secondary atmospheric variables. The latter, as well as all gas amounts except water vapor and carbon dioxide, are fixed here to reference values according to the 1976 US Standard Atmosphere (USSA). A large range of water vapor amounts is considered, between 0 (ideal dry atmosphere) to 4.5 cm (subtropical conditions), including the Mid-Latitude Summer (MLS) case (w = 2.87 cm). Additionally, the carbon dioxide concentration from the original USSA (330 ppmv) is revised upward to the more current value of 400 ppmv. All the other variables are varied to cover a wide range of possible conditions (Table 1) and to allow comparisons with earlier studies (e.g., Ballestrín and

Marzo, 2012). For the latter reason, the aerosol model corresponding to the Rural extinction profile and relatively turbid conditions, represented by a surface visibility (VIS) of 23 km, is specifically selected for the present study. At the other extreme, an ideal aerosol-free atmosphere is also considered. This option is interesting since the effect of water vapor effect on the transmission loss can then be clearly identified.

Table 1: Values of the MODTRAN inputs used to obtain the simulated database.

Inputs to MODTRAN	Values
Θ_Z (degrees)	0, 10, 20, 30, 40, 50, 60, 70, 80, 85, 90
H (m)	100, 200, 250
S (km)	0.15, 0.5, 1, 2, 4
w (cm)	0, 0.25, 1.42, 2.00, 2.87, 4.50
Aerosols	No aerosols, Rural VIS = 23 km

The solar radiation reflected by the mirror M, E_M, may be obtained by MODTRAN as:

$$E_M = \int_{0.28}^{4} \rho_\lambda T_{\lambda M} E_{\lambda 0} \mathrm{d}\lambda \quad (1)$$

where $E_{\lambda 0}$ is the Kurucz extraterrestrial spectral irradiance at 1 AU, $T_{\lambda M}$ is the atmospheric spectral transmittance for the sun-to-mirror path, which depends on the abundance of various atmospheric constituents, and thus varies over time, and ρ_λ is the mirror's spectral reflectance. The latter needs to be considered in order to evaluate its effect on the transmission losses of the reflected sunlight. Since this effect is relatively small, the reflectance is set here to 1 at all wavelengths for the sake of simplicity in this preliminary work. The integration limits, 0.28 μm and 4 μm, correspond to the range of wavelengths (λ) typically sensed by a pyrheliometer. Since the attenuation due to water vapor is the only one specifically evaluated here, all other atmospheric inputs are fixed at reasonable values, as noted above. The solar zenith angle is varied incrementally from 0º to 90º as shown in Table 1. Although solar power towers do not operate under large solar zenith angles, values higher than 80º are considered here anyway in order to analyze the trend of transmission losses under these extreme limits.

The irradiance reaching the tower receiver T (Fig. 2) is obtained using the slant-path option included in MODTRAN between two points at finite distance, i.e., the mirror and the receiver in the present case. MODTRAN calculations take into account the effects of the earth's sphericity and atmospheric refraction. The irradiance E_T is then obtained from:

$$E_T = \int_{0.28}^{4} \rho_\lambda T_{\lambda M-T} T_{\lambda M} E_{\lambda 0} \mathrm{d}\lambda \quad (2)$$

where, $T_{\lambda M\text{-}T}$ is the spectral transmittance for the mirror-to-tower slant path, and ρ_λ, $T_{\lambda M}$ and $E_{\lambda 0}$ correspond to the values needed to resolve Eq. (1).

Since the ratio E_T/E_M represents the broadband atmospheric transmittance between M and T, the broadband atmospheric transmission loss A may be readily derived using:

$$A = 1 - E_T/E_M. \quad (3)$$

2.2. Artificial neural network

Artificial neural networks are implemented here using a combination of custom-designed MATLAB functions (MatLab, 1999) in conjunction with several routines developed by Nørgaard (1997). A standard multilayer perceptron (MLP) architecture with three fully interconnected layers (input, hidden, and output) is employed, as shown in Fig. 3. The hyperbolic tangent transform is chosen as the nonlinear activation function in the hidden layer, and the identity function is selected as the activation function for the output layer. Such a network determines a non-linear mapping from an input vector (constituted of the MODTRAN inputs given in Table 1) to the output, i.e., the transmission loss A. The input and output vectors are parameterized by a set of network weights. These are referred to as hidden weights, w^h (weights connecting inputs to hidden neurons), and output weights, w^o (weights connecting hidden neurons to the output one). All weights are randomly initialized within the range (–0.5, 0.5). Among several existing training algorithms, a Gauss-Newton-based Levenberg-Marquartd method is selected due to its rapid convergence properties and robustness (Fletcher, 1987).

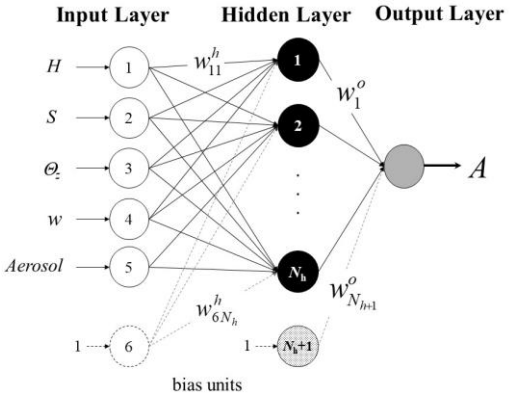

Fig. 3: Description of the ANN architecture used here.

3. Analysis and results

The influence on transmission loss of zenith angle, water vapor, and of some other variables is analyzed first. The ANN model results are presented in a second step. Figures 4 and 5 show the transmission loss A versus solar zenith angle for different values of water vapor content and slant ranges, respectively for the two contrasting turbidity scenarios detailed above: an ideal aerosol-free atmosphere (Fig. 4) and semi-hazy conditions corresponding to a visibility of 23 km (Fig. 5). In both Figures the tower height is H = 100 m.

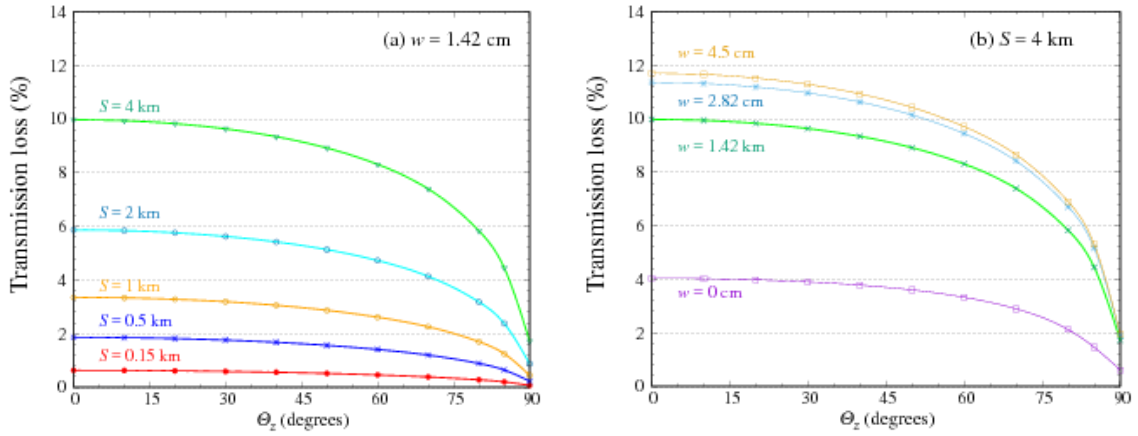

Fig. 4: Transmission loss for H = 100 m and an aerosol-free atmosphere, using: (a) a fixed w = 1.42 cm and several slant ranges, or (b) a fixed S = 4 km and several precipitable water values at ground level.

237

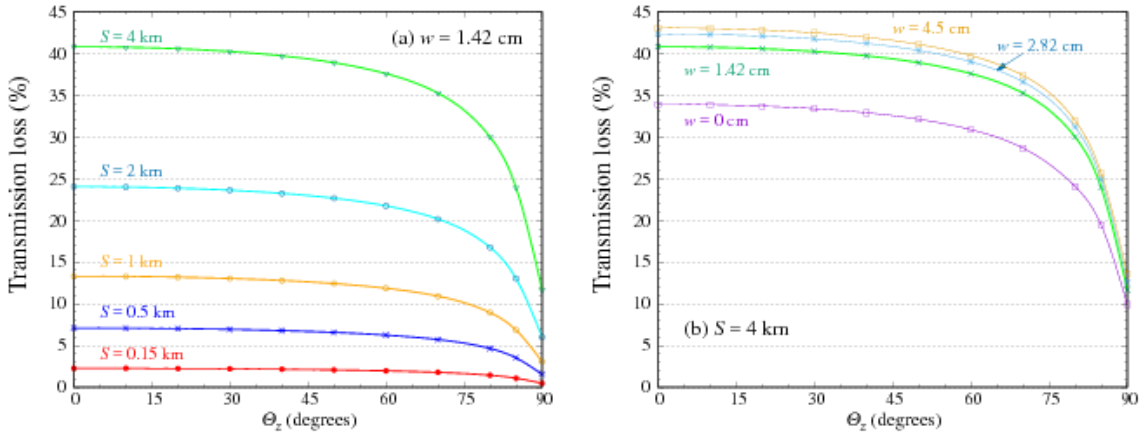

Fig. 5: Transmission loss for H = 100 m and semi-hazy conditions (VIS = 23 km), using: (a) a fixed w = 1.42 cm and several slant ranges, or (b) a fixed S = 4 km and several precipitable water values at ground level.

238 A is found to decrease sharply when zenith angle increases above ≈60°. More specifically,
239 A decreases from 5.6% to 4% when Θ_Z increases from 30º to 70º for a medium slant range
240 of 2 km, a constant precipitable water of 1.42 cm and an aerosol-free atmosphere. For a slant
241 range of 4 km, this loss increases up to 9.6% for Θ_Z = 30º, or 7.3% for Θ_Z = 70º. This means
242 that the pure effect of zenith angle is 2.3% when it varies between 30º and 70°. When haze
243 is present (23-km visibility), this specific effect is significantly stronger, reaching 3.6% for
244 S = 2 km and 5% for S = 4 km. On the other hand, this zenith angle effect is smaller (≈1%)
245 for short (< 1 km) slant ranges. The general decrease of A with increasing zenith angle is
246 caused by the saturation effect of water vapor absorption: when Θ_Z increases, so does the
247 total water vapor pathlength. This in turn depletes some wavelengths more or less
248 completely in the water vapor absorption bands, such as around 940 nm or 1400 nm. Thus,
249 the bulk of water vapor absorption occurs in the free atmosphere before the direct beam
250 reaches the mirror. After reflection on the mirror, the wavelengths that were already strongly
251 depleted before reflection cannot be depleted much more, even though there is substantial

water vapor between M and T. More specifically, this additional water cannot have any additional effect on the strongest spectral absorption lines that are already fully saturated, and can only have minimal effect on the moderately strong lines that are just partly saturated. Hence, A is less intense when Θ_Z is larger, since the total water vapor pathlength is also larger. Note that this saturation effect is slightly reduced if the tower height is increased, because the water vapor concentration decreases with height.

For a better understanding of the relationship between A and sun position, Fig. 6 displays the water vapor spectral transmittance corresponding to two solar positions: $\Theta_Z = 0^o$ and 90^o. Considering fixed values for the other parameters (w = 1.42 cm, H = 100 m, S = 4 km, and aerosol-free conditions), the transmission losses are 10% and 2%, respectively (Fig. 4). Figure 6a shows the spectral transmittances for each of the two path sections into which the entire solar beam's pathlength can be decomposed: from the top of atmosphere (TOA) to the mirror, $T_{\lambda M}$, and from the mirror to the receiver at the top of the tower, $T_{\lambda M\text{-}T}$. Fig. 6a shows how the spectral transmittance along the 4-km mirror-to-receiver slant path is slightly lower than that corresponding to the vertical TOA-to-mirror path ($T_{\lambda M\text{-}T} \leq T_{\lambda M}(0^o)$). The total spectral transmittance for this case, i.e., the product $T_{\lambda M}(0^o) \cdot T_{\lambda M\text{-}T}$, is shown in Fig. 6b (orange area). The red area corresponds to the water vapor's spectral transmittance. For this example, the broadband irradiances incident on the mirror and on the receiver are respectively $E_M(\Theta_Z = 0^o)$ = 1045 W/m^2 and E_T = 940.8 W/m^2. A significant energy loss of 10% is thus obtained. In the second case, it is found that $T_{\lambda M\text{-}T} > T_{\lambda M}(90^o)$, as a consequence of the larger sun-to-mirror path compared to the mirror-to-receiver path. The total spectral transmittance for the sun-to-receiver path is $T_{\lambda M}(90^o) \cdot T_{\lambda M\text{-}T} \approx T_{\lambda M}(90^o)$. The irradiances are then $E_M(\Theta_Z = 90^o)$ = 187 W/m^2 and E_T = 183.8 W/m^2, leading to energy losses of about 2%. This effect is similar to that corresponding to an increase the water vapor amount, as explained below. The reason is that the saturation effect is driven by the total slant column of water vapor, which can be approximated by $w/\cos(\Theta_Z)$ for Θ_Z less than ≈85°.

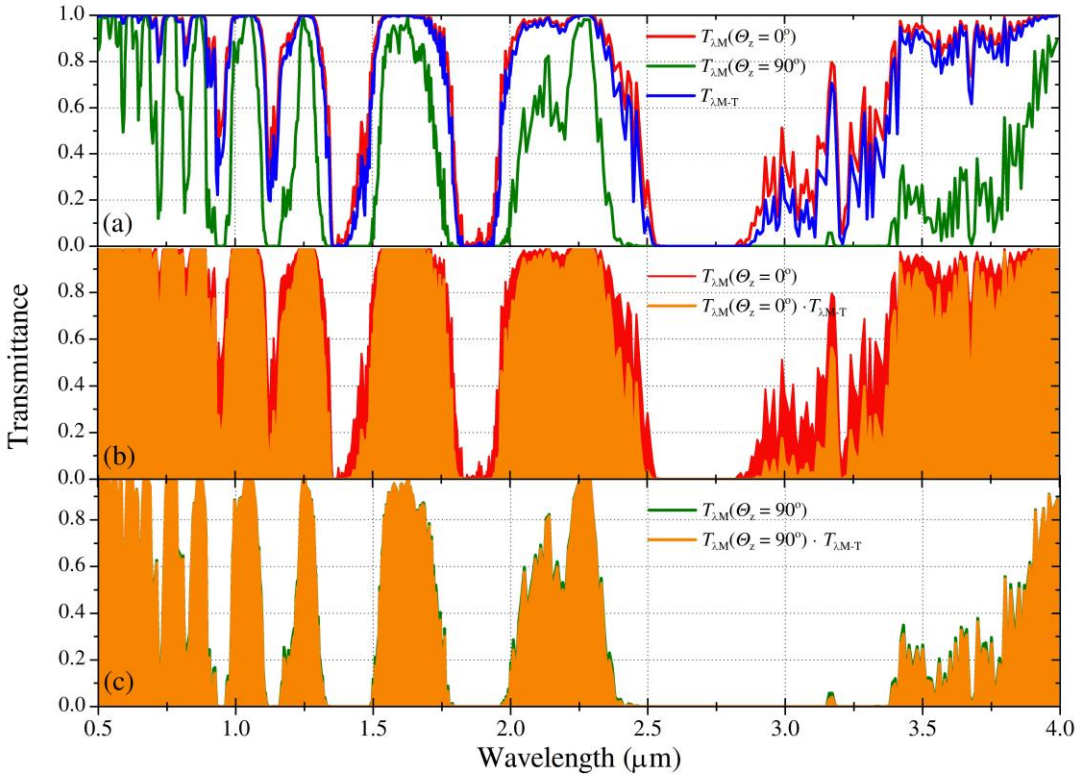

Fig. 6: Spectral transmittance T_λ for water vapor and different paths: (a) three paths are considered, (i) from the top of atmosphere (TOA) to the mirror at a zenith angle of 0º, $T_{\lambda M}(\Theta_z = 0^o)$; (ii) from TOA to the mirror at a zenith angle of 90º, $T_{\lambda M}(\Theta_z = 90^o)$; and (iii) from the mirror to the receiver at the tower, $T_{\lambda M\text{-}T}$; (b) $T_{\lambda M}(\Theta_z = 0^o)$ and the TOA-to-mirror-to-receiver path, $T_{\lambda M}(\Theta_z = 0^o) \cdot T_{\lambda M\text{-}T}$.; (c) $T_{\lambda M}(\Theta_z = 90^o)$ and the TOA-to-mirror-to-receiver path. Aerosol-free conditions with w = 1.42 cm, H = 100 m, and S = 4 km are used in all cases. In the bottom panels, the colored areas under the curves describe the saturation effect of water vapor on the total transmittance. In panel (b), the red area depicts the sun-to-mirror transmittance, whereas the orange color indicates the overall sun-to-mirror-to-receiver transmittance. The mirror-to-receiver path still reduces the initial transmittance (red area). This effect is larger for wavelengths beyond 1 μm. In panel (c), the orange area (similar to that for panel (b), but with Θ_z = 90º) is almost the same as the green area, which depicts the sun-to-mirror transmittance, thus indicating that the water vapor along the mirror-to-receiver path has virtually no effect on the total transmittance.

For an ideal atmosphere without aerosols or water vapor (w = 0), Fig. 4 shows the non-negligible effect of Rayleigh scattering (caused by air molecules) on the reflected solar energy for S = 4 km, leading to transmission losses of about 4%. The dependence of A on Rayleigh scattering is almost linear with slant range, generating transmission losses of ≈0.15% for S = 0.15 km, or ≈1% for S = 1 km, for instance.

Figure 4 also shows the significant attenuation effect of water vapor on transmitted solar radiation along the mirror-to-receiver path. In an aerosol-free atmosphere, the percent energy loss due to water vapor (combined with Rayleigh scattering) can be up to 3.5% over a short slant range (1 km) and 12% for a long slant range (4 km), assuming high humidity conditions (w = 4.5 cm). The results in Fig. 4 indicate that, under aerosol-free conditions (where Rayleigh scattering is the only cause of attenuation, apart from absorption), A

increases almost linearly with slant range. The latter result is also observed under turbid atmospheric conditions. Moreover, Fig. 4 reveals that the transmission loss due to water vapor alone reaches ≈6% for S = 4 km and low zenith angles, assuming w = 1.42 cm. This result is similar under a semi-hazy atmosphere (Fig. 5). In contrast, when precipitable water increases from 1.42 to 4.5 cm, the transmission losses only increase by 1–2%. This non-linear behavior is a consequence of the strong water vapor saturation effect, as explained above. This is also the reason why the transmission losses due to water vapor are relatively small, even under very humid conditions (w = 4.5 cm), in comparison with aerosol-induced losses, as the comparison of Figs. 4 and 5 reveals.

It is important to note that all the results above correspond to fixed rates of vertical decrease (or "scale heights") of the concentration of all atmospheric constituents, as specified by the USSA or MLS reference atmospheres. In the case of water vapor close to surface level, this assumed scale height is ≈2.2 km for USSA and ≈1.9 km for MLS. However, recent findings using high-resolution radiosonde soundings have shown that the water vapor scale height can vary rapidly (between typically 1 and 5 km) at any given site. The effect of this scale-height variability on the transmission loss is not negligible, as shown by Gueymard et al. (2016), and thus should be considered in future attenuation model developments.

3.1 ANN performance

To develop an ANN-based model, several free parameters must be fixed before the training stage. For the MLP-based model developed here, the only free parameter is the number of hidden units, N_h, since the number of inputs and outputs are fixed by design in a previous step. These ANN inputs (Fig. 3) correspond to the five variables used to obtain the simulated database by means of MODTRAN (Table 1): Θ_Z, H, S, w and VIS. The number of hidden neurons is chosen following a heuristic approach, where several networks with different values of N_h are trained and the best-performing network among them is selected. For this purpose, the synthetic database is randomly split into two sets, one for training the ANN and the other for testing the model. The latter amounts to ≈10% of the whole database. The ANN model's performance is analyzed in terms of both the root mean square difference (RMSD) and mean bias difference (MBD) between the estimated transmission losses and the MODTRAN-derived values. They are expressed as a percentage of the mean value of the latter.

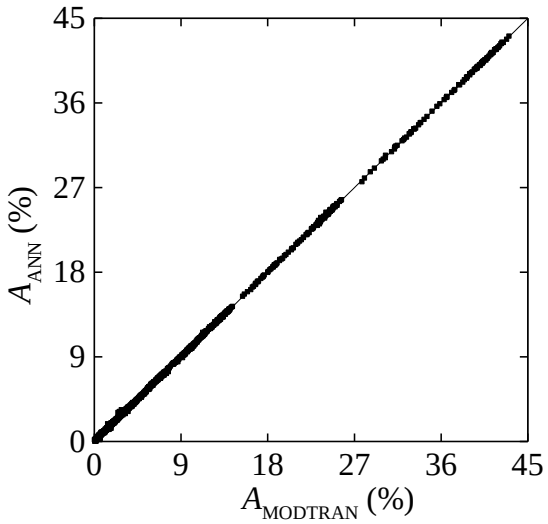

Fig. 7: Transmission loss *A* estimated by the ANN model compared to reference MODTRAN values.

Calculations show that the tested ANN models with $N_h > 30$ can generate very low RMSD (< 1%) and no bias, whereas a low amount of hidden neurons result in a larger RMSD. N_h is thus fixed to the "optimal" value just mentioned. Figure 7 shows the transmission loss estimated by the final ANN model compared to the original MODTRAN values. An almost perfect fit is observed, with an RMSD of only 0.8%. This result demonstrates the suitability of adding an appropriate ANN-based model to SPT simulation codes, to avoid the difficulties and computer time of operating a spectral code like MODTRAN.

4. Conclusions

In this work, the energy loss of direct normal irradiance is evaluated along its path from distant mirrors to the tower receiver of a large solar tower plant, focusing on the specific impact of water vapor. It is found that the concentration of surface water vapor along the mirror-to-tower path can lead to significant reductions (up to 12%) of the solar irradiance incident on the heliostat field. It is also shown that the water vapor saturation effect limits the increase in transmission loss when water vapor reaches the high-humidity conditions typical of tropical or subtropical regions, or when zenith angle exceeds ≈60°. The MODTRAN simulations elaborated here further indicate that transmission losses are not constant during the day since they depend on sun position. Daily variations of ≈4% can occur in the common operation of solar tower plants just due to this effect, at least when considering the farthest mirrors.

This contribution is apparently the first one in which the dependence of slant mirror-to-receiver attenuation on solar geometry is specifically mentioned. The analysis of an ideally pure, dry and aerosol-free atmosphere has also evidenced the non-negligible impact of molecular (Rayleigh) scattering along the mirror-to-receiver path, translating into a specific transmission loss of ≈1–4% for far-away mirrors, which increases linearly with the slant range. All these values slightly decrease if tower height increases, as an expected consequence of the air density reduction with height.

The modeling of transmission losses using two atmospheric variables (zenith angle and

precipitable water) and two variables for solar power plant design parameters (slant range and tower height) has been successfully solved using an artificial neural network (ANN) for two contrasting atmospheric turbidity conditions. The transmission losses estimated by the ANN model match those obtained by MODTRAN almost perfectly, and only require an easy and fast computation. The main advantages of this ANN approach are (i) the elimination of the complex and time-consuming use of MODTRAN; and (ii) the improvement in transmission loss parameterization compared to what was developed empirically decades ago. Thus, the present ANN model constitutes a valuable tool that could be added to existing solar tower plant design and operation simulation codes. Future work will examine the impact of varying vertical atmospheric profiles and different atmospheric turbidity conditions, to make this ANN model even more general.

5. Acknowledgments

The authors are grateful for the financial support provided by Spanish Project PRESOL "Forecast of solar radiation at the receiver of a solar power tower" with references 'ENE2014-59454-C3-1-R, ENE2014-59454-C3-2-R and ENE2014-59454-C3-3-R', which is funded by the Ministerio de Economía y Competitividad and co-financed by the European Regional Development Fund.

6. References

Alonso-Montesinos, J., Barbero, J., Polo, J., López, G., Ballestrín, J., Batlles, F.J., 2017. Impact of a Saharan dust intrusion over southern Spain on DNI estimation with sky cameras. Atmos. Environ. 170, 279-289. https://doi.org/10.1016/j.atmosenv.2017.09.040.

Ballestrín, J., Marzo, A., 2012. Solar radiation attenuation in solar tower plants. Sol. Energy 86, 388–392. http://dx.doi.org/10.1016/j.solener.2011.10.010.

Berk, A., Bernstein, L.S., Robertson, D.C., 1989. MODTRAN: A Moderate Resolution Model for LOWTRAN7. Report GL-TR-89-0122, Air Force Geophysical Laboratory, Hanscom, MA.

Bosch, J.L., López, G., Batlles, F.J., 2008. Daily solar irradiation estimation over a mountainous area using artificial neural networks. Renew. Energy 33, 1622–1628. https://doi.org/10.1016/j.renene.2007.09.012.

Cardemil, J.M., Starke, A.R., Scariot, V.K., Grams, I.L., Colle, S., 2014. Evaluating solar radiation attenuation models to assess the effects of climate and geographical location on the heliostat field efficiency in Brazil. Energy Proc. 49, 1288–1297. doi: 10.1016/j.egypro.2014.03.138.

Eissa, Y., Marpu, P.R., Gherboudj, I., Ghedira, H., Ouarda, T.B.M.J., Chiesa, M., 2013. Artificial neural network based model for retrieval of the direct normal, diffuse horizontal and global horizontal irradiances using SEVIRI images. Sol. Energy 89, 1–16.

Fletcher, R., 1987. Practical methods of optimization. John Wiley & Sons, Chichester.

Gueymard, C.A., López, G., Rapp-Arrarás, I., 2016. Atmospheric transmission loss in mirror-to-tower slant ranges due to water vapor. AIP Conf. Proc. 1850, 140010.

https://doi.org/10.1063/1.4984518.

López, G., Gueymard, C.A., 2007. Clear-sky solar luminous efficacy determination using artificial neural networks. Sol. Energy 81, 929–939. https://doi.org/10.1016/j.solener.2006.11.001.

López, G., Gueymard, C.A., Bosch, J.L., 2017. Evaluation of solar energy losses for the heliostat-to-receiver path of a tower solar plant for different aerosol models. Proc. Solar World Congress 2017, Abu Dhabi, UAE, International Solar Energy Society.

MatLab, 1999. The MathWorks, Inc. Natick, MA, USA.

Hanrieder, N., Wilbert, S., Mancera-Guevara, D., Buck, R., Giuliano, S., Pitz-Paal, R., 2017. Atmospheric extinction in solar tower plants – a review. Sol. Energy 152, 193–207. https://doi.org/10.1016/j.solener.2017.01.013

Nørgaard, M., 1997. Neural network based system identification toolbox. Technical Report 97-E-851, Department of Automation, Technical University of Denmark.

Polo, P., Ballestrín, J., Alonso-Montesinos, J., López, G., Barbero, J., Carra, E., Fernández-Reche, J., Bosch, J.L., Batlles, F.J., 2017. Analysis of solar tower plant performance influenced by atmospheric attenuation at different temporal resolutions related to aerosol optical depth. Sol. Energy 157, 803-810. http://dx.doi.org/10.1016/j.solener.2017.09.003.

Sengupta, M., Wagner, M., 2012. Estimating atmospheric attenuation in central receiver systems. ASME SunShot Symposium. 6th International Conference on Energy Sustainability. San Diego, CA, July 23–26.

Srikrishnan, V., Young, G.S., Witmer, L.Y., Brownson, J.R.S., 2015. Using multi-pyranometer arrays and neural networks to estimate direct normal irradiance. Sol. Energy 119, 531–542. https://doi.org/10.1016/j.solener.2015.06.004.

Tahboub, Z., Oumbe, A., Hassar, Z., Obaidli, A., 2014. Modeling of irradiance attenuation from a heliostat to the receiver of a solar central tower. Energy Proc. 49, 2405–2413. http://dx.doi.org/10.1016/j.egypro. 2014.03.255.

Takenaka, H., Nakajima, T.Y., 2011.Estimation of solar radiation using a neural network based on radiative transfer. J. Geophys. Res. 116, D08215, 1–26. doi:10.1029/2009JD013337.

Taylor, M., Kosmopoulos, P.G., Kazadzis, S., Keramitsoglou, I., Kiranoudis, C.T., 2015. Neural network radiative transfer solvers for the generation of high resolution solar irradiance spectra parameterized by cloud and aerosol parameters. J. Quant. Spectr. Rad. Transf. 168, 176–192. http://dx.doi.org/10.1016/j.jqsrt.2015.08.018.

Vittitoe, C.N., Biggs, F., 1978. Terrestrial propagation loss. Proc. ASES Solar Diversification Conf., Denver (CO, USA).